

# The combinations of hollow MoS<sub>2</sub> micro@nano-spheres: one-step synthesis, excellent photocatalytic and humidity sensing properties

Cite this: *J. Mater. Chem. C*, 2014, 2, 5422

Yinghua Tan,<sup>a</sup> Ke Yu,<sup>\*a</sup> Ting Yang,<sup>a</sup> Qingfeng Zhang,<sup>a</sup> Weitao Cong,<sup>a</sup> Haihong Yin,<sup>a</sup> Zhengli Zhang,<sup>a</sup> Yiwei Chen<sup>b</sup> and Ziqiang Zhu<sup>a</sup>

The combinations of hollow MoS<sub>2</sub> micro@nano-spheres were successfully fabricated through a one-step hydrothermal method. A possible growth mechanism was presented in detail based on time-dependent experimental facts. Besides, the photocatalytic activities of the samples were evaluated by monitoring the photodegradation of methylene blue (MB). The adsorption value of 150 mg g<sup>-1</sup> shows a strong adsorption capability in the dark. After irradiation for only 30 min, the remaining MB in solution is about 9.7%. Moreover, the humidity sensing properties of the samples were measured for the first time. The results revealed high sensitivity at high RH, small humidity hysteresis, fast response and recovery times, and good stability. The greatest sensitivity is 32.19 nF/% RH and the maximum hysteresis is ~6.3% RH. For humidity cycling of 17.2–89.5–17.2% RH, the response and recovery times are ~140 s and ~80 s, respectively. Capacitance fluctuations for one month are less than ±7% at various relative humidities (RHs).

Received 4th March 2014

Accepted 22nd April 2014

DOI: 10.1039/c4tc00423j

www.rsc.org/MaterialsC

## 1. Introduction

In recent decades, two-dimensional (2D) layered nanomaterials such as graphene have aroused increasing research interest in industrial and scientific fields because of their unique properties and wide potential applications.<sup>1–6</sup> MoS<sub>2</sub>, resembling graphene, a typical example of two-dimensional (2D) layered nanomaterials, has attracted great attention due to its layered structure, in which each layer consists of molybdenum atoms sandwiched between two layers of hexagonally close-packed sulfur atoms.<sup>7,8</sup> The adjacent atomic sandwiches are held together by weak van der Waals forces.<sup>9</sup> As a transition metal sulfide, MoS<sub>2</sub> possesses many excellent properties and is widely applied in many fields such as super solid lubricants,<sup>7</sup> lithium battery cathodes,<sup>10–12</sup> sensors,<sup>13–17</sup> photocatalysis,<sup>18–20</sup> hydrogen storage media,<sup>21,22</sup> dye-sensitized solar cells,<sup>23</sup> *etc.* To date, a great deal of effort has been devoted to the MoS<sub>2</sub> studies and all kinds of chemical and physicochemical methods, including hydrothermal methods,<sup>24,25</sup> gas-phase synthesis,<sup>26</sup> electrochemical deposition,<sup>27</sup> thermal decomposition,<sup>28</sup> chemical vapour deposition<sup>29</sup> and electrochemical based Li-intercalation method<sup>30</sup> have been put forward to synthesize MoS<sub>2</sub> with various morphologies, such as fullerene-like nanoparticles,<sup>26</sup> hollow microspheres,<sup>31</sup> nanotubes,<sup>21</sup> nanorods,<sup>32</sup> nanowires,<sup>33</sup>

and nanoflowers.<sup>24</sup> But it is still a challenge to fabricate various novel combinations of MoS<sub>2</sub> with controlled sizes *via* a facile and effective method. Herein, we first report the fabrication of hollow MoS<sub>2</sub> micro@nano-spheres through a one-step hydrothermal method. Moreover, the growth process and a possible formation mechanism of the samples were preliminarily presented on the basis of the experimental facts by adjusting the reaction time.

Generally, the overall photocatalytic activities of semi-conductive materials are mainly decided by three factors: (1) the adsorption ability of photocatalysts, (2) the separation and transporting rate of the photogenerated holes and electrons for the existence of active surfaces (sites) in catalysts, and (3) photoabsorption ability in the available light energy region.<sup>34</sup> MoS<sub>2</sub> with various morphologies previously reported has prospective applications in photocatalysis and the energy gap of MoS<sub>2</sub> nanomaterials is close to 1.78 eV, with a strong absorption in the visible light region to improve the utilization of sunlight.<sup>19,35</sup> Therefore, it is certainly worth investigating the photocatalytic activities of these hollow MoS<sub>2</sub> micro@nano-spheres. Besides, MoS<sub>2</sub> is also an ideal candidate material for gas sensors, such as hydrogen sensors, which is evidenced by theoretical results<sup>14</sup> and recent experiments.<sup>36</sup> However, little research on the humidity sensing properties of the MoS<sub>2</sub> nanostructure has been deeply reported so far.

Hence the photocatalytic activities of the novel hollow MoS<sub>2</sub> micro@nanocrystals are examined in our paper. The reasons for the strong adsorption capability and excellent photocatalytic activity for organic pollutants under visible light illumination are discussed. Furthermore, the humidity sensing

<sup>a</sup>Key Laboratory of Polar Materials and Devices (Ministry of Education of China), Department of Electronic Engineering, East China Normal University, Shanghai, 200241, P. R. China. E-mail: yk5188@263.net; Fax: +86-21-54345198; Tel: +86-21-54345198

<sup>b</sup>Department of Physics, East China Normal University, Shanghai, 200241, P. R. China

performances of the MoS<sub>2</sub>-based sensors are investigated for the first time and the results indicate that the sensors possess pronounced sensitivity in a high RH environment, very small humidity hysteresis, fast response and recovery time, and good stability. A theoretical explanation of the humidity sensing properties is also given in our research.

## 2. Experimental section

### 2.1 Synthesis of hollow MoS<sub>2</sub> micro@nano-spheres

In our experiments, all chemicals were of analytical grade and used directly without further purification. The combinations of hollow MoS<sub>2</sub> micro@nano-spheres were fabricated through a one-step hydrothermal route in Teflon-lined autoclaves. The preparation procedure is described as follows: 0.4 g thioacetamide (C<sub>2</sub>H<sub>5</sub>NS) and 0.2 g sodium molybdate (Na<sub>2</sub>MoO<sub>4</sub>·2H<sub>2</sub>O) as Mo and S sources, respectively, were dissolved in 60 mL deionized water to form a transparent solution, and then 0.5 g oxalic acid (H<sub>2</sub>C<sub>2</sub>O<sub>4</sub>) was added into the above solution to adjust the pH value. After magnetic stirring for 30 min, a homogeneous solution was obtained and transferred into a Teflon-lined stainless-steel autoclave. The autoclave was heated at 200 °C for 22 h in an electric oven. After naturally being cooled down to room temperature, black precipitates were collected, washed sequentially by sonication for 10 min with deionized water and ethanol several times, and finally dried at 60 °C for 6 h to obtain the black powders. To obtain MoS<sub>2</sub> with good crystallinity, the as-prepared samples were annealed under an atmosphere of Ar at 800 °C for 2 h in a conventional tube furnace.

### 2.2 Characterization

The crystal structure of the products was characterized by X-ray diffraction (XRD, Bruker D8 Advance diffractometer) with Cu K $\alpha$  radiation ( $\lambda = 1.5418$  Å). The diffraction patterns were collected in the  $2\theta$  scanning range of 10–80° with 0.02° per step. The morphologies and structures of the samples were examined by field emission scanning electron microscopy (FESEM, JEOL-JSM-6700F) at an accelerating voltage of 20 kV, and transmission electron microscopy (TEM, Jeol, JEM-2100) at an accelerating voltage of 200 kV. All measurements of the as-prepared samples were carried out at room temperature. The samples for TEM analysis were obtained by adding a drop of the colloidal solution onto a standard holey carbon-coated copper grid. The grids were dried in air at room temperature.

### 2.3 Photocatalytic measurements

The photocatalytic properties of the as-prepared samples were investigated by the degradation of methylene blue (MB) aqueous solution. The concentration of the extracted MB solution was tested by monitoring the absorbance at the major absorption peak (663 nm). Before illumination, the suspension containing as-prepared MoS<sub>2</sub> (0.01 g) and 120 mL of 20 mg L<sup>−1</sup> MB aqueous solution was treated by sonication for 6 min and then magnetically stirred in the dark for 20 min to ensure the establishment of the adsorption/desorption equilibrium. 4 mL

of the suspension was withdrawn and clarified by centrifugation at 800 rpm for 10 min to remove the residual catalyst. Then the clarified solution was analyzed using a UV-vis spectrophotometer (UNICO 2802) to evaluate the adsorption ability. For photocatalytic degradation measurements, the suspension was illuminated with an 18 W daylight lamp (20 cm above the reactor) used as a solar-simulated light source. To minimize the heat effect, the reactor was implemented in a big glass container and cooled by flowing water at room temperature. The aliquots (4 mL) of the suspension were clarified and analysed after 10 min periodic intervals of irradiation, during the total 60 min irradiation time. For comparison, various initial concentrations of MB (25 mg L<sup>−1</sup>, 15 mg L<sup>−1</sup>, and 10 mg L<sup>−1</sup>) were used in the adsorption tests.

### 2.4 Preparation of sensors for humidity measurement

A MoS<sub>2</sub>-based humidity sensor is constructed with an interdigitated-type electrode and a MoS<sub>2</sub> film on the surface of a glass sheet substrate, as shown in the inset of Fig. 7(c). The glass sheet substrate (12 cm × 16 cm × 0.5 cm) was cleaned using a sonication bath for 5 min, and the interdigitated-type silver paste electrodes with electrode gaps of width ~0.5 mm and ~3 mm were deposited on the glass substrate. The Ag electrodes are the electrodes of the double-layer capacitance. The MoS<sub>2</sub> suspension was dispersed by the ultrasonic method and deposited by dip coating on the glass substrate with the electrode to form a thin film as a humidity sensing layer. Then the foregoing glass substrate was dried at 50 °C for 6 h to form a humidity sensor. The controlled humidity environments, 23, 43, 57, 75, 80, 85, and 93% RH, were achieved using saturated aqueous solution of CH<sub>3</sub>COOK, K<sub>2</sub>CO<sub>3</sub>, NaBr, NaCl, KBr, KCl, and KNO<sub>3</sub> at room temperature, respectively. These saturated salt solutions were placed in JKZ1 Radiosonde Ground Check to provide uniform and stable humidity environments. Different humidity environments result in different effective dielectric constants which lead to different capacitances. In the capacitance measurement, the equipment we used was the Precision LCR Meter TH2817A with a frequency of 100 kHz from China Tonghui.

## 3. Results and discussion

### 3.1 Structure characterization

The XRD patterns of annealed and unannealed samples are shown in Fig. 1(a). It is obvious that the as-prepared MoS<sub>2</sub>, after being annealed under Ar at 800 °C, exhibits high crystallinity compared with unannealed samples. The observed diffraction peaks at  $2\theta = 14.4^\circ$ ,  $33.1^\circ$ ,  $39.7^\circ$  and  $58.5^\circ$  can be assigned to the (002), (100), (103) and (110) planes of the hexagonal phase MoS<sub>2</sub> with lattice constants  $a = b = 0.316$  nm, and  $c = 1.229$  nm (molybdenite, JCPDS card no. 37-1492), respectively. Besides the very weak diffraction peaks at  $2\theta = 37^\circ$  and  $53.5^\circ$  can be suitably indexed to monoclinic MoO<sub>3</sub>, which reveals that the annealed sample is MoS<sub>2</sub> containing trace amounts of MoO<sub>3</sub> impurity. This may be due to the existence of trace oxygen in the process of high-temperature annealing. The XRD pattern of the as-

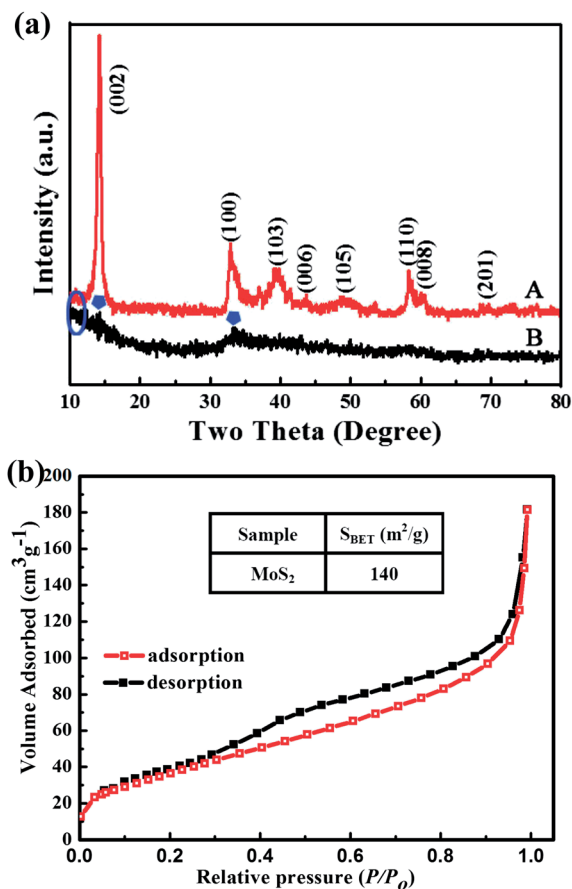


Fig. 1 (a) X-ray patterns of (A) annealed samples and (B) unannealed samples. (b) Nitrogen adsorption/desorption isotherms of hollow MoS<sub>2</sub> micro@nano-spheres. The table in the inset is the  $S_{\text{BET}}$  for the samples.

obtained unannealed samples only displays two weak diffraction peaks, (002) and (100), and the other characteristic peaks do not appear, which indicates poor crystallinity of the samples and makes it difficult to identify their phase. This poor-stacked structure can be explained by the tensile force and randomness of the amorphous samples.<sup>31</sup> In addition, it is worth noticing that a new diffraction peak, marked with blue line circles in Fig. 1(a)B, is found near  $2\theta = 10^\circ$  which could not be indexed to MoS<sub>2</sub>. The new peak may be due to the reflection from two adjacent single-layer amorphous MoS<sub>2</sub> (ref. 37) or the greater distance of unannealed MoS<sub>2</sub> layers,<sup>11</sup> which is possibly associated with the strain/stress caused by the bending and folding of the amorphous layers.<sup>38</sup> While the annealed samples exhibit high crystallinity and a strong diffraction peak (002) at  $2\theta = 14.4^\circ$  with an interlayer spacing of 0.62 nm, as shown in Fig. 1(a) A, which indicates that the layered MoS<sub>2</sub> grows well along the *c* axis. Therefore, the crystallinity of the MoS<sub>2</sub> samples prepared by the hydrothermal route could be improved by annealing at high temperature and readjustment of the achieved strain/stress to lead to the disappearance of the diffraction peak near  $\sim 10^\circ$ . From the N<sub>2</sub> adsorption/desorption isotherm (Fig. 1(b)), a distinct hysteresis loop is identified at a relative pressure of 0.1–0.9, demonstrating the presence of a mesoporous structure,

which leads to a Brunauer–Emmett–Teller (BET) surface area of  $140 \text{ m}^2 \text{ g}^{-1}$ .

The size and morphology of the as-synthesized MoS<sub>2</sub> were primarily characterized by SEM images at different magnifications. In Fig. 2(a) and (b), it is very obvious that the obtained products are composed of microspheres and nanospheres with diameters of  $\sim 1 \mu\text{m}$  and  $\sim 200 \text{ nm}$ , respectively, called combinations of hollow MoS<sub>2</sub> micro@nano-spheres. Additionally, every microsphere is dispersedly surrounded by nanospheres. The numbers of these microspheres and nanospheres are relatively coordinated in the hydrothermal process, which makes this micro@nano-structure look uniform and coordinated. The insets of Fig. 2(b) and (c) clearly show the surfaces of these nanospheres and microspheres. The rough surfaces with abundant weak burrs are scraggly. The typical contact interface between a microsphere and a nanosphere distinctly confirms that microspheres and nanospheres grow into holes during the hydrothermal process as shown in the inset of Fig. 2(c). As presented in Fig. 2(c) and (d), several broken microspheres indicate that microspheres are hollow and the thicknesses of the microsphere shell are about 40 nm, only about a fourteenth

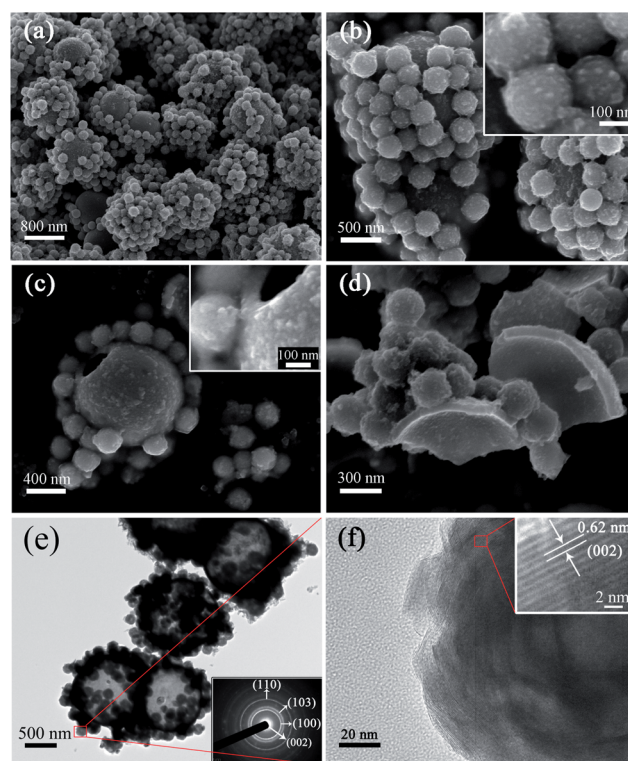


Fig. 2 (a) Low magnification SEM image. (b) Medium magnification SEM image. The inset is the high magnification SEM image of several typical nanosphere surfaces. (c) The SEM image of a microsphere surface. The inset is the HRSEM of the typical contact interface between a microsphere and a nanosphere. (d) The SEM image of several broken microspheres. (e) The TEM image of the typical samples. The lower inset is the corresponding selected area electron diffraction (SAED) pattern. (f) The high-resolution TEM image of a nanosphere, the red rectangular area in (e). The upper inset is the HRTEM image corresponding to the red rectangular area.



of the diameter of a hollow microsphere, which demonstrates that the microsphere shells are very thin and frangible.

The structure of the samples was further characterized by TEM and high-resolution TEM (HRTEM) images. Fig. 2(e) presents a typical TEM image of several microspheres surrounded by nanospheres. The significant contrast between the edges and centres of the microspheres further confirms the hollow structure feature. Fig. 2(f) is the HRTEM image of the red rectangular area in Fig. 2(e). Some defects and faults are observed on the surface of the nanosphere, which lead to the rough surfaces with abundant weak burrs and pits. The rough surfaces of microspheres, resembling nanospheres, should also be due to the abundant defects and faults, which can increase the specific surface area to improve various performances, such as adsorption capacity, photocatalytic activity, *etc.* It should be noted that the nanospheres obviously consist of several layers. There is a distinct difference between the middles and edges in the nanosphere structure. Compared with the edges, the internal streaks were observably less and even none, suggesting that the nanospheres' structure is virtually several thin nested spherical shells. This structure is similar to 'Russian doll' or 'onion' structure<sup>31</sup> and very crucial to understand its formation mechanism. The HRTEM image in the inset, corresponding to the red rectangular area in Fig. 2(f), presents the lattice fringes of the samples with the well-defined crystal structure, and the lattice spacing, assigned to the (002) plane, is about 0.62 nm. The inset in Fig. 2(e) illustrates that the corresponding selected area electron diffraction (SAED) rings arise from the stacking of MoS<sub>2</sub> with different crystallographic orientations. The central bright spot corresponds to the (002) plane and the observed separated diffraction rings correspond to the (100), (103) and (110) planes, respectively, which is consistent with the XRD result.

### 3.2 The time-dependent possible formation mechanism

Generally, the formation of nanomaterials with different morphologies may be related to the characteristics of amorphous primary particles and nucleation under different reaction conditions.<sup>39</sup> Besides, the reaction time of the hydrothermal process is crucial to the growth of morphologies. Therefore, the temporal evolution of the products is monitored by TEM and SEM to shed light on the morphological evolution and formation mechanism of the hollow MoS<sub>2</sub> micro@nano-spheres. First, we proposed a possible growth mechanism for nanospheres in Scheme 1, which was drawn based on the TEM of temporal evolution in Fig. 3. Scheme 1 actually reveals a similar Ostwald ripening self-assembly process with a fast nucleation of

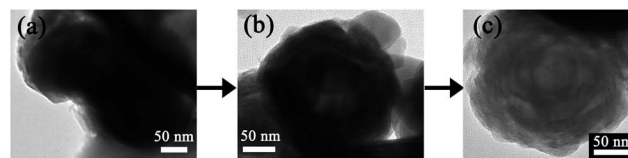
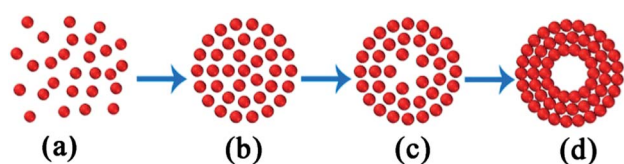


Fig. 3 TEM images aimed at disclosing the growth process of nanospheres by interrupting the reaction at different times: (a) 2 h, (b) 6 h, and (c) 10 h.

amorphous primary particles.<sup>40</sup> Prior to heating, numerous amorphous primary MoS<sub>2</sub> nanoparticles, symbolized by the red globules in Scheme 1, were generated in the reaction solution. After heating to a certain temperature, these amorphous primary MoS<sub>2</sub> nanoparticles spontaneously and quickly aggregated into evacuating solid spheres and then evolved with respectively layered spherical shells. The amorphous nanoparticles located in the centre of the solid spheres were loose and less dense than those in the outer parts. When prolonging the reaction time, it was found that the amorphous MoS<sub>2</sub> particles in the internal layered spherical shells were transferred to the outer parts, resulting in a small void in the centre and shorter distance between the spherical layers. With the time sequentially increasing, the central void became largely dense and well-crystallized layered spherical shells were located at the outer parts. The 'onion' structure with a little cavity was finally formed.

Additionally, to further gain insight into the growth process and formation mechanism of the hollow micro@nano-spheres, keeping other typical parameters unchanged, time-dependent experiments at different reaction times (2 h, 6 h, 10 h, 14 h, 18 h, and 22 h) were conducted and monitored by SEM images of the obtained products in Fig. 4. When the reaction time was 2 h, microspheres cannot be found and the product only consisted of nanospheres and abundant granules (Fig. 4(a)) which may be the amorphous primary particles that form microspheres. More granules may be lost during the washing process. Prolonging the reaction time to 6 h, many small cambered pieces were observed in Fig. 4(b) and the high-magnification SEM image in the inset of Fig. 4(b) clearly shows a typical cambered piece with small fissures and the loose aggregation of granules. When the reaction time was increased to 10 h, the trend of cambered growth became more obvious. As illustrated in Fig. 4(c), the size of the cambered surface was about a third of the microsphere. After the time reached 14 h, the size of the cambered shell became greater than a half of the microsphere. The thin edges of a typical cambered shell reveal the growth direction in the inset of Fig. 4(d). Meanwhile, some nanospheres attached on these cambered surfaces to grow together in Fig. 4(d), where black particles were the amorphous primary granules without being washed away to form MoS<sub>2</sub> microspheres. With further increase of the reaction time to 18 h, the shell almost grew into a sphere except for a small hole and more nanospheres sequentially attached on the newly grown spherical shell, which is observed in Fig. 4(e). The high-magnification SEM image in the inset of Fig. 4(e) clearly shows a typical small hole on the microsphere. After the time reached 22 h, hollow MoS<sub>2</sub>



Scheme 1 The schematic demonstration of the proposed formation mechanism of MoS<sub>2</sub> nanospheres.

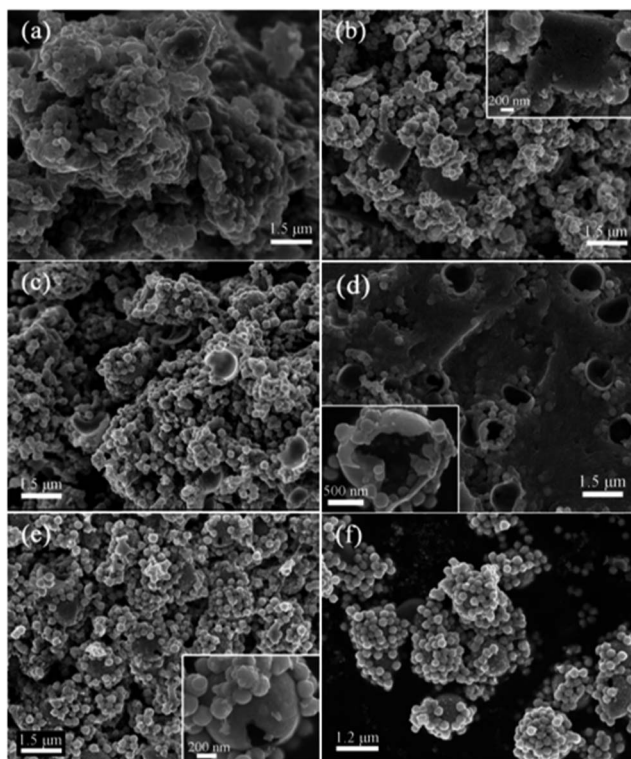
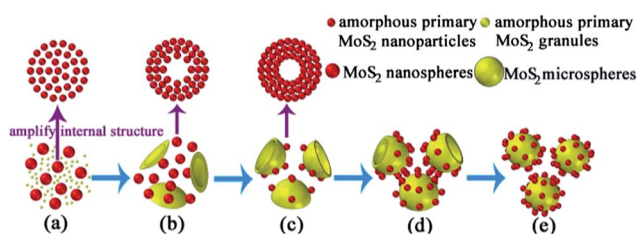


Fig. 4 SEM images aimed at disclosing the growth process of  $\text{MoS}_2$  micro@nano-spheres by interrupting the reaction at different times: (a) 2 h, (b) 6 h, (c) 10 h, (d) 14 h, (e) 18 h, and (f) 22 h.

micro@nano-spheres were eventually formed as shown in Fig. 4(f). In the growth process, the reaction time is the most significant controlling factor.

Based on our experimental facts, the proposed schematic of the growth process of the hollow micro@nano-spheres is depicted in Scheme 2. In the first stage, the previously discussed evacuating solid nanospheres and the amorphous primary  $\text{MoS}_2$  granules, symbolized by big red balls and smaller yellow balls, respectively, were initially formed at a temperature of  $200^\circ\text{C}$  for 2 h. Different from amorphous primary  $\text{MoS}_2$  particles generated at room temperature to form nanospheres, these amorphous primary  $\text{MoS}_2$  granules were generated during high temperature *via* the reaction of the remainder solute and in a stronger acidic solution because of the increasing hydrolysis of undecomposed oxalic acid. Due to the effect of low concentration, high temperature, and stronger acidic solution, these



Scheme 2 The schematic demonstration of the proposed formation mechanism of the hollow  $\text{MoS}_2$  micro@nano-spheres.

amorphous granules with different surface free energies did not aggregate into small spheres through the Ostwald ripening process. Instead, the earlier amorphous granules were spontaneously oriented and aggregated to form many tiny cambered pieces with an amorphous and poorly crystallized phase. With the increase of reaction time, the later amorphous granules, formed during the continually decreasing concentration of the solute, were transferred toward the previous cambered pieces and grew along with the cambered pieces, as reported by K. H. Hu *et al.*,<sup>41</sup> which resulted in the growth of cambered pieces further to larger pieces. Simultaneously, nanospheres were formed on the surfaces of these cambered pieces due to the reassembly aggregation and distribution between nanospheres and the new growing cambered surfaces. As the reaction time was sequentially prolonged and the aging process continued, the evacuating solid nanosphere gradually evolved into the 'onion' structure and these cambered pieces nearly became hollow microspheres. Meanwhile, nanospheres attached on the new growth cambered surfaces. Finally, the combinations of hollow  $\text{MoS}_2$  micro@nano-spheres were perfectly formed. On the basis of the above results, we reach a conclusion that the formation mechanism of nanospheres is similar to the Ostwald ripening with a fast self-assembly nucleation and a slow evolution process. Nevertheless, the growth process of the microspheres was the growth of amorphous granules along with the spherical surfaces. The two kinds of growth processes are simultaneous. Eventually, microspheres and nanospheres grow into well-dispersed holes.

### 3.3 Photocatalytic activities

Methylene blue (MB) with a major absorption peak at 663 nm is one of the most common contaminants in industrial waste water and used to estimate the adsorption abilities and photo-degradation activities of the as-prepared samples. The changes in the absorption spectra of the extracted MB solution in the presence of the  $\text{MoS}_2$  samples are shown in Fig. 5(a). For comparison, the supernatant of  $\text{MoS}_2$  solution without MB was obtained (green line in Fig. 5(a)), accounting for the absorption spectra (750–900 nm) above zero except for the main peaks. The continuous reduction of the absorption intensity at 663 nm indicates the gradually decreasing concentration of MB with the extended irradiation time. The dependency of the degradation rate on the irradiation time is revealed in Fig. 5(b), where  $C$  and  $C_0$  stand for the remnants and initial concentration of MB, respectively. A comparison photodegradation experiment on the degradation of pristine MB solution without photocatalysts was performed and there was almost no photocatalytic decolorization of MB after irradiation for 1 h as shown by the black line in Fig. 5(b). Therefore,  $\text{MoS}_2$  plays an essential role in efficient dye degradation under visible light illumination. Before the light irradiation, the mixed solution of  $\text{MoS}_2$  and MB was stirred in the dark to establish the adsorption/desorption equilibrium of MB on the sample surfaces. Dramatically, the remaining MB in solution is about 37.6%, indicating that the  $\text{MoS}_2$  samples present strong adsorption ability towards MB, with the adsorption value of  $150 \text{ mg g}^{-1}$  in the dark. This is

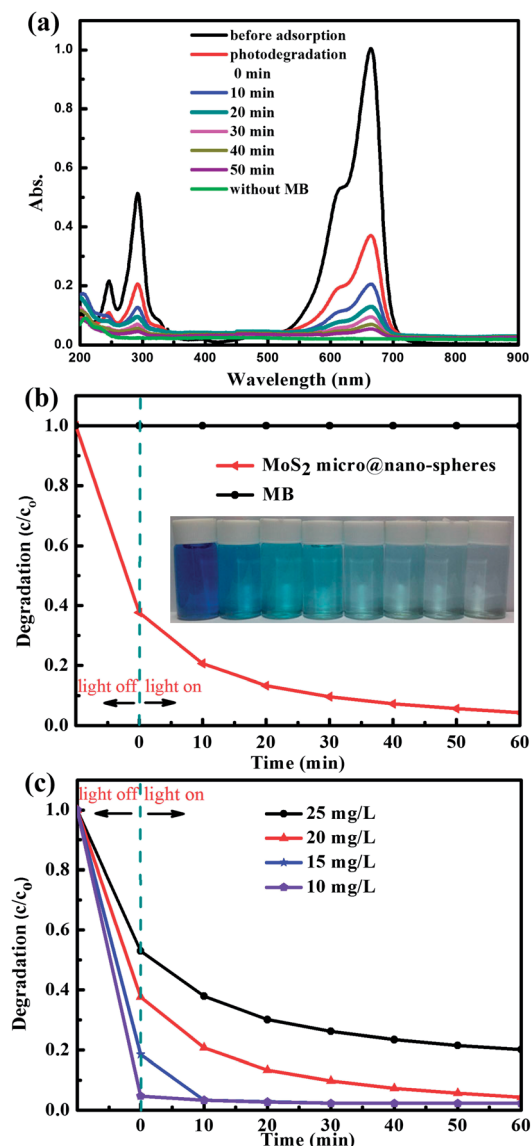
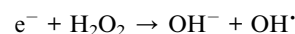
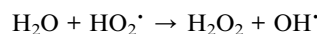
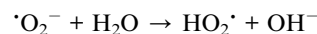
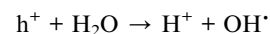
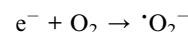


Fig. 5 (a) Absorption spectra of the MB solution under visible light irradiation in the presence of the MoS<sub>2</sub> samples. (b) Degradation rates of MB with and without the photocatalyst as a function of irradiation time. (c) Degradation rates of MB with the photocatalyst versus the different initial concentrations.

possibly due to the large specific surface area which can adsorb the abundant dye molecules.<sup>18</sup> Moreover, according to the previous data, the MoS<sub>2</sub> samples evidently exhibit very high photodegradation activities in the photodegradation of MB. After irradiation for only 30 min, the  $C/C_0$  rapidly dropped to 9.7% and MB was almost completely degraded under 60 min light irradiation. This result is also consistent with the colour change of the suspension from blue to colourless. In order to determine the favourable exploitation rate and reveal the effect of the initial concentration of MB on the degradation rate, Fig. 5(c) shows a comparison of the various initial concentrations of MB aqueous solutions. It can be clearly seen that the degradation rate gradually decreased when the initial concentration increased. Interestingly, when the initial concentration

of MB is less than 20 mg L<sup>-1</sup> the strong adsorption ability plays a major role in removing dye molecules. Photodegradation capacity is not fully utilized which implies a lower utilization rate for the photocatalyst.

The excellent photocatalytic performance of the as-prepared samples is attributed to not only the large specific surface area but also the scraggly surfaces of MoS<sub>2</sub> micro@nano-spheres with abundant weak burrs and a strong absorption in the visible light region. It is generally accepted that the large specific surface area can improve the adsorption capacity for dye molecules and bring more unsaturated surfaces' coordination sites exposed to the MB molecules. To the best of our knowledge, the rim and edge sites of MoS<sub>2</sub> are the active sites for the HDS reaction based on the 'rim-edge' mode.<sup>42</sup> As shown in Fig. 6(a) and (b), every S atom coordinates two Mo atoms on the S-edge and every Mo atom coordinates four S atoms on the Mo-edge. Mo- and S-edges with dangling bonds are unstable and would strongly interact with positively charged MB molecules.<sup>43</sup> Herein, the scraggly surfaces with abundant defects and faults can provide vast rim and edge active sites for the degradation of MB. Additionally, Fig. 6(c) shows that MoS<sub>2</sub> samples have an observable absorbance at ~440 nm and ~470 nm in the visible light region. Thurston and Wilcoxon also reported that the absorption peak of MoS<sub>2</sub> ( $d = 4.5$  nm) is at ~470 nm.<sup>35</sup> Electrons from the valence band of MoS<sub>2</sub> absorb visible light and transfer to the conduction band to produce separated electron-hole pairs. The photoexcited electrons were scavenged by the oxygen in the water and valence band holes were adsorbed by water molecules, which can form hydroxyl radicals (<sup>•</sup>OH) to photo-oxidize organic molecules.<sup>35</sup> A possible mechanism accounting for <sup>•</sup>HO production can be written as:<sup>44</sup>



Furthermore, the existence of broken microspheres cannot be excluded among the samples because of the thin spherical

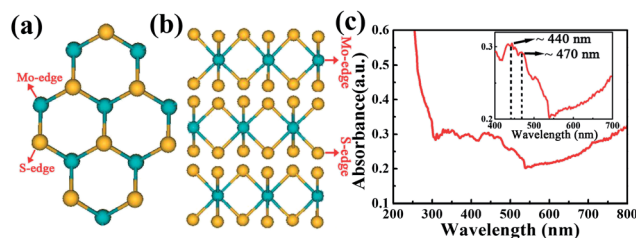


Fig. 6 (a) The top view of the hexagonal MoS<sub>2</sub> crystallite exposing Mo- and S-edges. (b) The side view of the hexagonal MoS<sub>2</sub> crystallite exposing Mo- and S-edges. (c) UV-vis spectra of the samples. The inset shows an expanded view for the visible light region.



shells, which brings about more rim and edge active sites and improves the degradation rate of MB. We believe that this kind of attractive material with high adsorption abilities and excellent photocatalytic performances will have promising application in the water treatment to remove toxic heavy metal ions and degrade dye pollutants.

### 3.4 Humidity sensing properties

The humidity sensing properties of the MoS<sub>2</sub>-based sensor were evaluated through discussing humidity sensitivity, hysteresis, response and recovery time, and stability at various relative humidities (RHs). The sensor capacitance as a function of RH is

presented by the red line in Fig. 7(a) during the adsorption process. It can be observed that the output capacitance exponentially increases with the RH. When RH changed from 17.2% to 52.8%, the relative capacitance only increased from 89.25 pF to 96.36 pF, a fairly small increment. Nevertheless, as RH varied from 71.8% to 89.5%, the relative capacitance dramatically rose from 0.504 nF to 6.01 nF, exhibiting pronounced sensitivity in a high RH environment. To quantitatively illustrate its humidity sensitivity, the sensitivity is defined as  $\Delta C/\Delta RH(\%)$ , the ratio of the change in output capacitance to the change in RH, and the sensitivity values at different RHs can be seen clearly in the inset of Fig. 7(a). It is found that the greatest sensitivity is 32.19 nF/% RH (at RH = 89.5%) which confirms high sensitivity in a high RH environment. Hysteresis is an important parameter for evaluating the performance of a humidity sensor. Fig. 7(a) also illustrates the hysteresis properties of the as-fabricated sensor by increasing the RH from 10% to 98% for water molecules adsorption and then decreasing back to 10% for water molecules desorption. From the narrow humidity loop curve, the differences between output capacitances in the adsorption and desorption process are obviously small under all humidity conditions. The maximum hysteresis was  $\sim 6.3\%$  RH that occurred at 71.8% RH which exhibits good reversible characteristics. Further the dynamic testing of the sensing device was carried out to investigate more parameters including response and recovery time, and reproducibility at 25 °C. Fig. 7(b) shows the time-dependent response and recovery curves (corresponding to water molecule adsorption and desorption processes). During humidity cycling of 17.2–71.8–17.2% RH the response and recovery time (defined as the time required to reach 95% of the final steady capacitance value) are  $\sim 90$  s and  $\sim 110$  s, respectively. For 17.2–89.5–17.2% RH cycling, the response time and recovery time are  $\sim 140$  s and  $\sim 80$  s, respectively. The results indicate fast response behaviour for humidity sensing. Moreover, three cycles demonstrate good reproducibility of the sensor. To test the stability, the sensor was exposed in air for 30 days and the measurements were repeated every 2 days at different RHs. It can be observed that the capacitance fluctuations are less than  $\pm 7\%$  in the relevant humidity region and the sensitivity variation for one month is also small, as shown in the inset of Fig. 7(a), which directly confirms the good stability and reliability. Therefore, MoS<sub>2</sub> micro@nano-spheres are expected to be potential materials for high humidity sensors.

The humidity sensitive performances of MoS<sub>2</sub>-based humidity sensors may be mainly attributed to the large specific surface area of the samples, which can increase the moisture adsorption capacity and facilitate the release of water molecules. The humidity sensing mechanism of the MoS<sub>2</sub> samples is the charge transfer between H<sub>2</sub>O molecules and MoS<sub>2</sub> surfaces, which has been previously reported by Q. Yue *et al.*<sup>14</sup> A large number of H<sub>2</sub>O molecules are continually physisorbed on the MoS<sub>2</sub> surfaces with the increment of RH, and H<sub>2</sub>O molecules are preferably adsorbed on the top of hexagons (in Fig. 8(a)).<sup>14,45</sup> Electron charges are sequentially transferred from the MoS<sub>2</sub> surfaces to H<sub>2</sub>O molecules as charge acceptors (in Fig. 8(b)). Consequently, the free electrons on the MoS<sub>2</sub> film decrease

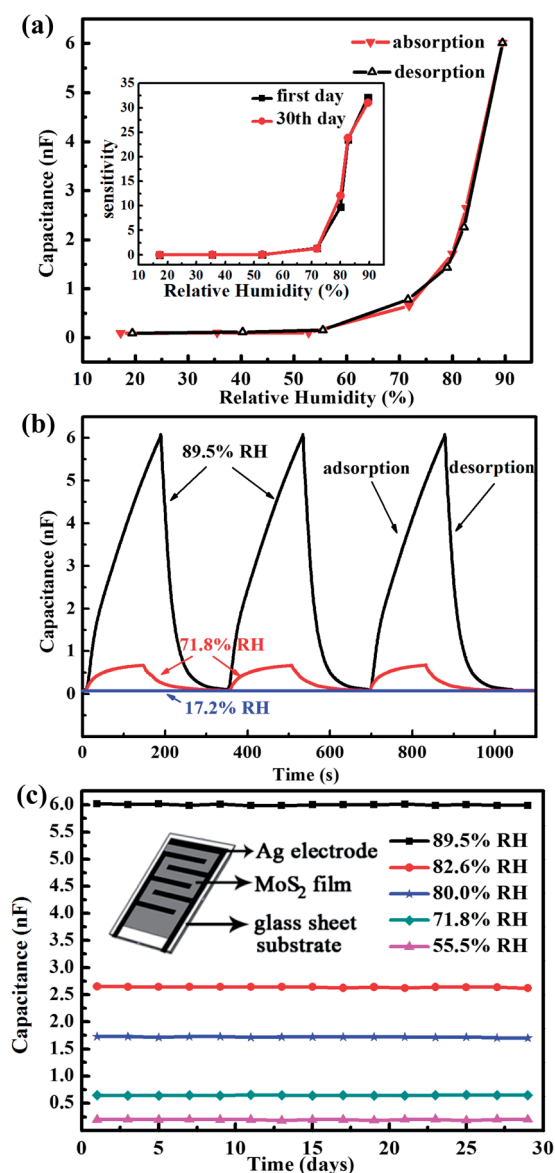


Fig. 7 (a) Experimental capacitance–RH response and hysteresis loop curve of the as-fabricated sensor. The inset is the defined sensitivity at different RHs. (b) The response and recovery times under humidity cycling of 17.2–71.8–17.2% RH and 17.2–89.5–17.2% RH. (c) Capacitance variations at various RH levels in 30 days. The inset is a schematic diagram of the as-fabricated sensor.

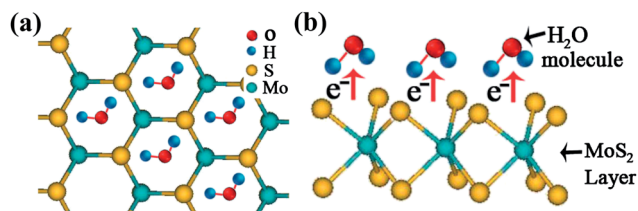


Fig. 8 (a) The top view of the most favorable configurations for H<sub>2</sub>O molecules on the MoS<sub>2</sub> film. (b) The schematic image of the humidity sensing mechanism.

during the adsorption process, which increases the dielectric constant. As we know, the capacitance is positively proportional to the dielectric constant and the reciprocal of the thickness of the double layer electrodes. The thickness of the double layer electrodes is constant in the testing process. So the capacitance increased with the dielectric constant. At low RH, the probability of contact between water molecules and MoS<sub>2</sub> surfaces is low<sup>46</sup> and water molecules cannot form continuous water layers. Hence, the transfer of H<sub>2</sub>O or H<sub>3</sub>O<sup>+</sup> on the discontinuous water layer is difficult<sup>47</sup> and the sensor exhibits lower sensitivity. As the RH is increased, several serial water layers emerge on the MoS<sub>2</sub> surfaces and the physisorbed water can be ionized by an electrostatic field into abundant H<sub>3</sub>O<sup>+</sup> as charge carriers.<sup>48</sup> The rapid transfer of H<sub>2</sub>O or H<sub>3</sub>O<sup>+</sup> on the free water layers possibly transports electrons to the outer water layers *via* the conductivity, sharply accelerating the decrease of the electron density on the MoS<sub>2</sub> surfaces, which results in high sensitivity at high RH. Furthermore, the dielectric constant of hydrated water is 2.2 and free water is 78, which also raise the output capacitance and enhance the sensor sensitivity at high RH.<sup>48</sup>

## 4. Conclusion

In summary, the combinations of hollow MoS<sub>2</sub> micro@nano-spheres were successfully synthesized through a one-step hydrothermal method. A possible formation mechanism was discussed. In addition, the samples possess strong adsorption capabilities in the dark and excellent photocatalytic activities under visible light illumination. We believe this kind of attractive material will have promising application in the water treatment to remove toxic heavy metal ions and degradation of dye pollutants. The humidity sensing properties of the samples were measured for the first time, and the results indicated high sensitivity at high RH, small humidity hysteresis, fast response and recovery times, and good stability. A humidity sensing mechanism is also given in our research. Therefore, the hollow MoS<sub>2</sub> micro@nano-spheres can be a promising candidate for high humidity sensor applications in the future.

## Acknowledgements

The authors acknowledge financial support from the NSF of China (Grant no. 61204018, 61274014), Innovation Research Project of Shanghai Education Commission (Grant no. 13zz033), Education Committee of Jiangsu Province (Grant no.

12KJD510011), and Project of Key Laboratory of Polar Materials and Devices (Grant no. KFKT2014003).

## Notes and references

- 1 C. N. Rao, A. K. Sood, K. S. Subrahmanyam and A. Govindaraj, *Angew. Chem., Int. Ed. Engl.*, 2009, **48**, 7752–7777.
- 2 R. Mas-Balleste, C. Gomez-Navarro, J. Gomez-Herrero and F. Zamora, *Nanoscale*, 2011, **3**, 20–30.
- 3 X. Cao, Z. Yin and H. Zhang, *Energy Environ. Sci.*, 2014, DOI: 10.1039/c4ee00050a.
- 4 Q. He, S. Wu, Z. Yin and H. Zhang, *Chem. Sci.*, 2012, **3**, 1764–1772.
- 5 Z. Yin, J. Zhu, Q. He, X. Cao, C. Tan, H. Chen, Q. Yan and H. Zhang, *Adv. Energy Mater.*, 2014, DOI: 10.1002/aenm.201300574.
- 6 X. Huang, Z. Zeng, Z. Fan, J. Liu and H. Zhang, *Adv. Mater.*, 2012, **24**, 5979–6004.
- 7 M. R. Hilton, R. Bauer, S. V. Didziulis, M. T. Dugger, J. M. Keem and J. Scholhamer, *Surf. Coat. Technol.*, 1992, **53**, 13–23.
- 8 M. Chhowalla, H. S. Shin, G. Eda, L.-J. Li, K. P. Loh and H. Zhang, *Nat. Chem.*, 2013, **5**, 263–275.
- 9 R. Tenne, L. Margulis, M. Genut and G. Hodes, *Nature*, 1992, **360**, 444–446.
- 10 S. Ding, D. Zhang, J. S. Chen and X. W. Lou, *Nanoscale*, 2012, **4**, 95–98.
- 11 S. K. Park, S. H. Yu, S. Woo, B. Quan, D. C. Lee, M. K. Kim, Y. E. Sung and Y. Piao, *Dalton Trans.*, 2013, **42**, 2399–2405.
- 12 X. Cao, Y. Shi, W. Shi, X. Rui, Q. Yan, J. Kong and H. Zhang, *Small*, 2013, **9**, 3433–3438.
- 13 Q. He, Z. Zeng, Z. Yin, H. Li, S. Wu, X. Huang and H. Zhang, *Small*, 2012, **8**, 2994–2999.
- 14 Q. Yue, Z. Shao, S. Chang and J. Li, *Nanoscale Res. Lett.*, 2013, **8**, 1–7.
- 15 C. Zhu, Z. Zeng, H. Li, F. Li, C. Fan and H. Zhang, *J. Am. Chem. Soc.*, 2013, **135**, 5998–6001.
- 16 S. Wu, Z. Zeng, Q. He, Z. Wang, S. J. Wang, Y. Du, Z. Yin, X. Sun, W. Chen and H. Zhang, *Small*, 2012, **8**, 2264–2270.
- 17 H. Li, Z. Yin, Q. He, H. Li, X. Huang, G. Lu, D. W. H. Fam, A. I. Y. Tok, Q. Zhang and H. Zhang, *Small*, 2012, **8**, 63–67.
- 18 W. Zhou, Z. Yin, Y. Du, X. Huang, Z. Zeng, Z. Fan, H. Liu, J. Wang and H. Zhang, *Small*, 2013, **9**, 140–147.
- 19 K. H. Hu, X. G. Hu, Y. F. Xu and X. Z. Pan, *React. Kinet., Mech. Catal.*, 2010, **100**, 153–163.
- 20 Z. Yin, B. Chen, M. Bosman, X. Cao, J. Chen, B. Zheng and H. Zhang, *Small*, 2014, DOI: 10.1002/sml.201400124.
- 21 J. Chen, S. L. Li and Z. L. Tao, *J. Alloys Compd.*, 2003, **356–357**, 413–417.
- 22 J. Chen, N. Kuriyama, H. Yuan, H. T. Takeshita and T. Sakai, *J. Am. Chem. Soc.*, 2001, **123**, 11813–11814.
- 23 G. Yue, J. Wu, Y. Xiao, M. Huang, J. Lin and J.-Y. Lin, *J. Mater. Chem. A*, 2013, **1**, 1495.
- 24 Q. Zhang, K. Yu, B. Zhao, Y. Wang, C. Song, S. Li, H. Yin, Z. Zhang and Z. Zhu, *RSC Adv.*, 2013, **3**, 10994.



- 25 C.-B. Ma, X. Qi, B. Chen, S. Bao, Z. Yin, X.-J. Wu, Z. Luo, J. Wei, H. Zhang and H. Zhang, *Nanoscale*, 2014, DOI: 10.1039/c3nr04975b.
- 26 A. Zak, Y. Feldman, V. Alperovich, R. Rosentsveig and R. Tenne, *J. Am. Chem. Soc.*, 2000, **122**, 11108–11116.
- 27 E. A. Ponomarev, M. Neumann-Spallart, G. Hodes and C. Lévy-Clément, *Thin Solid Films*, 1996, **280**, 86–89.
- 28 C. M. Zelenski and P. K. Dorhout, *J. Am. Chem. Soc.*, 1998, **120**, 734–742.
- 29 X. Wang, H. Feng, Y. Wu and L. Jiao, *J. Am. Chem. Soc.*, 2013, **135**, 5304–5307.
- 30 Z. Zeng, Z. Yin, X. Huang, H. Li, Q. He, G. Lu, F. Boey and H. Zhang, *Angew. Chem., Int. Ed.*, 2011, **50**, 11093–11097.
- 31 G. Li, C. Li, H. Tang, K. Cao, J. Chen, F. Wang and Y. Jin, *J. Alloys Compd.*, 2010, **501**, 275–281.
- 32 M. A. Albiter, R. Huirache-Acuna, F. Paraguay-Delgado, J. L. Rico and G. Alonso-Nunez, *Nanotechnology*, 2006, **17**, 3473–3481.
- 33 W.-J. Li, E.-W. Shi, J.-M. Ko, Z.-Z. Chen, H. Ogino and T. Fukuda, *J. Cryst. Growth*, 2003, **250**, 418–422.
- 34 Z. Ai, L. Zhang, S. Lee and W. Ho, *J. Phys. Chem. C*, 2009, **113**, 20896–20902.
- 35 T. R. Thurston and J. P. Wilcoxon, *J. Phys. Chem. B*, 1998, **103**, 11–17.
- 36 B. Miremadi, R. Singh, S. R. Morrison and K. Colbow, *Appl. Phys. A*, 1996, **63**, 271–275.
- 37 Z. Wang, L. Ma, W. Chen, G. Huang, D. Chen, L. Wang and J. Y. Lee, *RSC Adv.*, 2013, **3**, 21675.
- 38 M. Wang, G. Li, H. Xu, Y. Qian and J. Yang, *ACS Appl. Mater. Interfaces*, 2013, **5**, 1003–1008.
- 39 H. Shi, K. Yu, F. Sun and Z. Zhu, *CrystEngComm*, 2012, **14**, 278–285.
- 40 H. C. Zeng, *Curr. Nanosci.*, 2007, **3**, 177–181.
- 41 K. H. Hu and X. G. Hu, *Mater. Sci. Technol.*, 2009, **25**, 407–414.
- 42 M. Daage and R. R. Chianelli, *J. Catal.*, 1994, **149**, 414–427.
- 43 V. M. Kogan and P. A. Nikulshin, *Catal. Today*, 2010, **149**, 224–231.
- 44 S. Li, K. Yu, Y. Wang, Z. Zhang, C. Song, H. Yin, Q. Ren and Z. Zhu, *CrystEngComm*, 2013, **15**, 1753–1761.
- 45 F. K. Perkins, A. L. Friedman, E. Cobas, P. M. Campbell, G. G. Jernigan and B. T. Jonker, *Nano Lett.*, 2013, **13**, 668–673.
- 46 H. Yin, K. Yu, Z. Zhang, M. Zeng, L. Lou and Z. Zhu, *Electroanalysis*, 2011, **23**, 1752–1758.
- 47 W.-D. Lin, H.-M. Chang and R.-J. Wu, *Sens. Actuators, B*, 2013, **181**, 326–331.
- 48 H. Bi, K. Yin, X. Xie, J. Ji, S. Wan, L. Sun, M. Terrones and M. S. Dresselhaus, *Sci. Rep.*, 2013, **3**, 2714.